ARTICLE

# Generalized Gaussian distribution-based pre-stack inversion: A case study of channel sands in the Lianggaoshan Formation, Sichuan Basin

**Meng Yuan\*** , **Zhiwei Miao** , **Lei Pan** , **Jianlong Su** , **and Chang Sun**

Exploration and Research Institute, Sinopec Exploration Company, Chengdu, Sichuan, China

(This article belongs to the *Special Issue: Geophysical Inversion and Intelligent Prediction Technologies for Complex Hydrocarbon Reservoirs*)

**\*Corresponding author:**
Meng Yuan
(yuanm.ktnf@sinopec.com)

## Abstract

Tight sandstone channel systems occur in the second member of the Lianggaoshan Formation in the Sichuan Basin. These channels predominantly exhibit single bright-spot reflections on seismic sections. Due to the limited resolution of post-stack data and the constraints of attribute dimensionality, drilling results reveal complex internal lithological assemblages and pronounced lateral heterogeneity within these channels. Traditional post-stack methods struggle to effectively characterize internal channel details, thereby hindering subsequent exploration planning and reserve evaluation. To address these challenges, this study develops a pre-stack seismic inversion workflow based on generalized Gaussian distribution (GGD) prior constraints, aiming to enhance the identification and prediction of complex channel sand bodies. First, pre-stack amplitude versus offset (AVO) response analysis was conducted using typical wells to determine the effective incident angle range. By integrating optimal angle stacked data and AVO attribute extraction, the accuracy of characterizing the lateral distribution of channels was improved. Subsequently, a low-frequency facies-controlled model was constructed by integrating AVO attributes with elastic parameters. GGD prior constraints were incorporated into the pre-stack elastic parameter inversion, enabling detailed prediction of internal channel architecture. This technique yielded promising results in the Fuxing Block and was successfully validated in the Bazhong Block. It effectively enhanced the accuracy of identifying and predicting complex channels, providing technical support for the exploration, deployment, and resource evaluation of Jurassic tight sandstone channels in the Sichuan Basin.

*Keywords:* Channel sandstone; Lianggaoshan Formation; Amplitude versus offset attribute; Generalized Gaussian distribution; Low-frequency facies-controlled model

## 1. Introduction

The Jurassic tight sandstones in the Sichuan Basin host substantial oil and gas resources.[1] Fluvial sandstone reservoirs in Jurassic continental strata have become a key target for recent hydrocarbon exploration. Both the China National Petroleum Corporation and Sinopec have reported large-scale geological reserves in this area, confirming promising

exploration prospects and significant resource potential in Jurassic tight sandstones.[2] The Lianggaoshan Formation, a Middle Jurassic ($J_2$l) sedimentary unit, is characterized by a delta-lacustrine depositional system. During the middle to late depositional stages of its second member ($J_2l^2$) through the third member ($J_2l^3$), the basin experienced continuous lacustrine regression, dominated by delta-front deposits. This period resulted in the development of multiple episodes of subaqueous distributary channel sand bodies, which are vertically stacked, laterally interconnected, and exhibit a banded distribution pattern. These sand bodies are widely distributed in the Fuxing Block (southeastern Sichuan) and the Bazhong Block (northeastern Sichuan).

As critical reservoirs for hydrocarbon accumulation, channel sand bodies have long been a primary focus of seismic exploration due to their distinct sedimentary features and distribution patterns.[3] To better understand the seismic response of channel sands, Li *et al.*[4] developed numerous thin-interbed convolution models based on typical channel sedimentary patterns to investigate the seismic reflection characteristics of sand-mud interbeds. Similarly, Li *et al.*[5] applied wave equation-based methods to analyze the seismic reflection characteristics of channel sandstones, examining the relationship between seismic reflections and sedimentation patterns from the perspective of wavelength interference. Other researchers have systematically studied the response characteristics of various continental thin-interbed configurations, revealing that post-stack seismic reflections vary significantly with changes in sandstone-to-mudstone stacking patterns, relative position, and thickness.[6,7] Collectively, these studies have advanced the understanding of seismic responses of channel systems under different sedimentary backgrounds by analyzing how sand-mud combinations and thickness variations manifest in post-stack seismic data.

For channels characterized by substantial width, thick individual sand bodies, and distinct seismic responses, post-stack seismic methods remain effective for delineating their planar distribution. Various techniques applied to channel sand prediction have yielded satisfactory results.[8,9] In terms of seismic identification, approaches such as spectral decomposition and waveform clustering based on post-stack data have been successfully employed to map channel distribution.[10,11] The seismic expression of thin-interbed sand bodies has been enhanced through 90° phase rotation or phase spectrum decomposition, while post-stack inversion methods, including sparse pulse and waveform indication inversion, have been utilized for channel sand prediction through P-impedance inversion.[12] Amplitude versus offset (AVO) characteristic analysis has enabled the identification of incident angles favorable for

channel sand detection, with partial stacking techniques improving the identification of subtle channels.[13-15] The development and implementation of these identification and prediction technologies have demonstrated their effectiveness across multiple blocks, showing broad applicability.

With the progression of channel sandstone exploration from simple to complex types, growing evidence suggests that post-stack seismic data face inherent limitations in resolving the detailed response characteristics of intricate channel systems due to constraints in seismic resolution. Conventional post-stack seismic attributes likewise show limited capability in enhancing the identification accuracy of internal architectural details within such complex channels.[16] Post-stack inversion methods are often inadequate for quantitatively characterizing the heterogeneity and spatial complexity of these channels, typically exhibiting low resolution in predicting sand-mud interbedded intervals. In response, significant research efforts have been directed toward AVO inversion to improve the accuracy of lithology and reservoir prediction.[17-25] However, AVO inversion itself is susceptible to noise contamination, leading to considerable uncertainties in results and challenges in achieving reliable and stable solutions.[26] To mitigate this, AVO inversion commonly integrates prior information within a Bayesian framework to enhance stability. Currently adopted prior distributions include Gaussian, Cauchy, Huber, and modified Cauchy distributions. Applications based on these prior assumptions have demonstrated positive outcomes across various blocks, showing appreciable applicability in practice.[27]

Horizontal well drilling from Fuxing Block in the Sichuan Basin reveals that the Lianggaoshan Formation channels exhibit multi-phase vertical stacking, extensive sandstone-mudstone interbedding, and pronounced lateral heterogeneity. The tuning effect further destabilizes the seismic response of single bright-spot channels, while the limited resolution of post-stack seismic data proves inadequate for detailed reservoir characterization. These limitations result in significant multi-solution uncertainty in channel prediction, consequently constraining optimal horizontal well placement and impeding efficient reserve development in the block.

To address these challenges, this study develops a comprehensive pre-stack seismic workflow for characterizing complex channel systems in the Jurassic Lianggaoshan Formation. The methodology comprises three key stages. First, pre-stack AVO analysis of horizontal well data from the Fuxing Block is employed to identify the optimal incident angle range for detecting lithological variations. Selective angle stacking within this range

enhances the response characteristics of single bright-spot channels and improves channel distribution mapping. Second, AVO attribute analysis identifies gradient attributes as particularly sensitive to lithological changes. Extraction of these attributes significantly improves the accuracy of channel characterization. Finally, within a Bayesian framework, we extend the conventional Gaussian before a more adaptable generalized Gaussian distribution (GGD). After validating its statistical suitability with well data, we integrate the pre-stack angle gathers with AVO attributes to construct a geologically constrained low-frequency model. This facilitates pre-stack inversion that effectively resolves internal channel architecture. Application of this workflow to the $J_2l^2$ reservoirs in the Fuxing Block yielded significant improvements in channel prediction, with subsequent successful validation in the Bazhong Block confirming its robustness. This approach provides reliable technical support for reservoir evaluation and development optimization of complex channel systems in the Sichuan Basin.

## 2. Overview of the study area

Recent exploration studies confirmed that the Jurassic Lianggaoshan Formation in both the Fuxing Block (southeastern Sichuan Basin) and Bazhong Block (northeastern Sichuan Basin) developed under sedimentary conditions favorable for deltaic meandering river channel sandstones. Vertically, the formation comprises three distinct members: from base to top, the first ($J_2l^1$), second ($J_2l^2$), and third ($J_2l^3$) members. This vertical succession records a complete transgressive-regressive cycle, which promoted the development of multiple phases and types of vertically superimposed channel systems. In addition, the presence of numerous hydrocarbon source centers within the formation provides favorable conditions for near-source hydrocarbon accumulation (Figure 1).

In the absence of dedicated exploration wells targeting channel sandstones in the Lianggaoshan Formation, Sinopec drilled Well FL1 in the Fuxing Block to evaluate the second member ($J_2l^2$). The well penetrated a 26.5-m sandstone interval, and production testing yielded promising results, with an average daily output of 13,100 m³ of gas and 10.4 m³ of oil. This success confirms the presence of large-scale channel sandstone development in the $J_2l^2$ and highlights the reserve potential of the Lianggaoshan Formation. To further assess the scale of accumulation in this channel system, Well FL101 was subsequently drilled, encountering a 21.9-m sandstone layer in the same member. Well-seismic calibration confirmed that the sandstone in Well FL101 belongs to the same channel phase as that encountered in Well FL1. Post-stack seismic profiles across both wells showed a consistent

"peak-top and trough-bottom" reflection configuration, characterized by a single bright-spot wavelet, indicating relatively uniform lithology and lateral continuity of the channel sandstone (Figure 2).

To enable effective production from the $J_2l^2$ channel sandstones, a sidetracked horizontal well (FL101HF) was drilled from the Well FL101 platform along a favorable azimuth targeting distinct bright-spot anomalies. The actual trajectory largely traversed the flanks of these seismic amplitude features. Drilling results revealed predominantly pure sandstone in the first half of the horizontal section, transitioning to pronounced sand-mud interbedding in the second half. This marked lateral lithological variation diverges significantly from pre-drill seismic interpretations (Figure 3), demonstrating substantial heterogeneity within the channel system. The integration of data from vertical Well FL101 and horizontal sidetrack FL101HF confirms that the uniform bright-spot channel contains significant internal heterogeneity, with laterally discontinuous sandstone distribution. This complexity remained unresolved in conventional post-stack seismic data due to its limited vertical resolution, which proves inadequate for characterizing the intricate lithological variations and internal architecture of the channel fill.

## 3. Methodology

To address the limitations of post-stack seismic data in characterizing complex channel sandstones within the $J_2l^2$ member, this study developed a dedicated pre-stack seismic prediction workflow. The methodology, outlined below, comprised three sequential steps designed to leverage the full information content of pre-stack data for enhanced lithological discrimination.

(i) AVO response analysis. AVO forward modeling of various lithological intervals, calibrated with horizontal well data, was performed. The comparative analysis of synthetic and actual seismic gathers revealed the amplitude-variation-with-angle behavior, pinpointing the incident angle range that is diagnostic of lithological changes.

(ii) AVO attribute extraction: Guided by the AVO response, an optimal approximation of the Zoeppritz equation was applied to the $J_2l^2$ seismic data. The resultant intercept or gradient attribute that most effectively characterized channel internal geometry was extracted for subsequent analysis.

(iii) Pre-stack seismic inversion: A low-frequency, facies-controlled model was constructed by integrating the well-derived interpolation model with the diagnostic AVO attributes, thereby reconciling vertical detail with lateral trends. Finally, a pre-stack inversion employing GGD prior constraints was implemented to produce
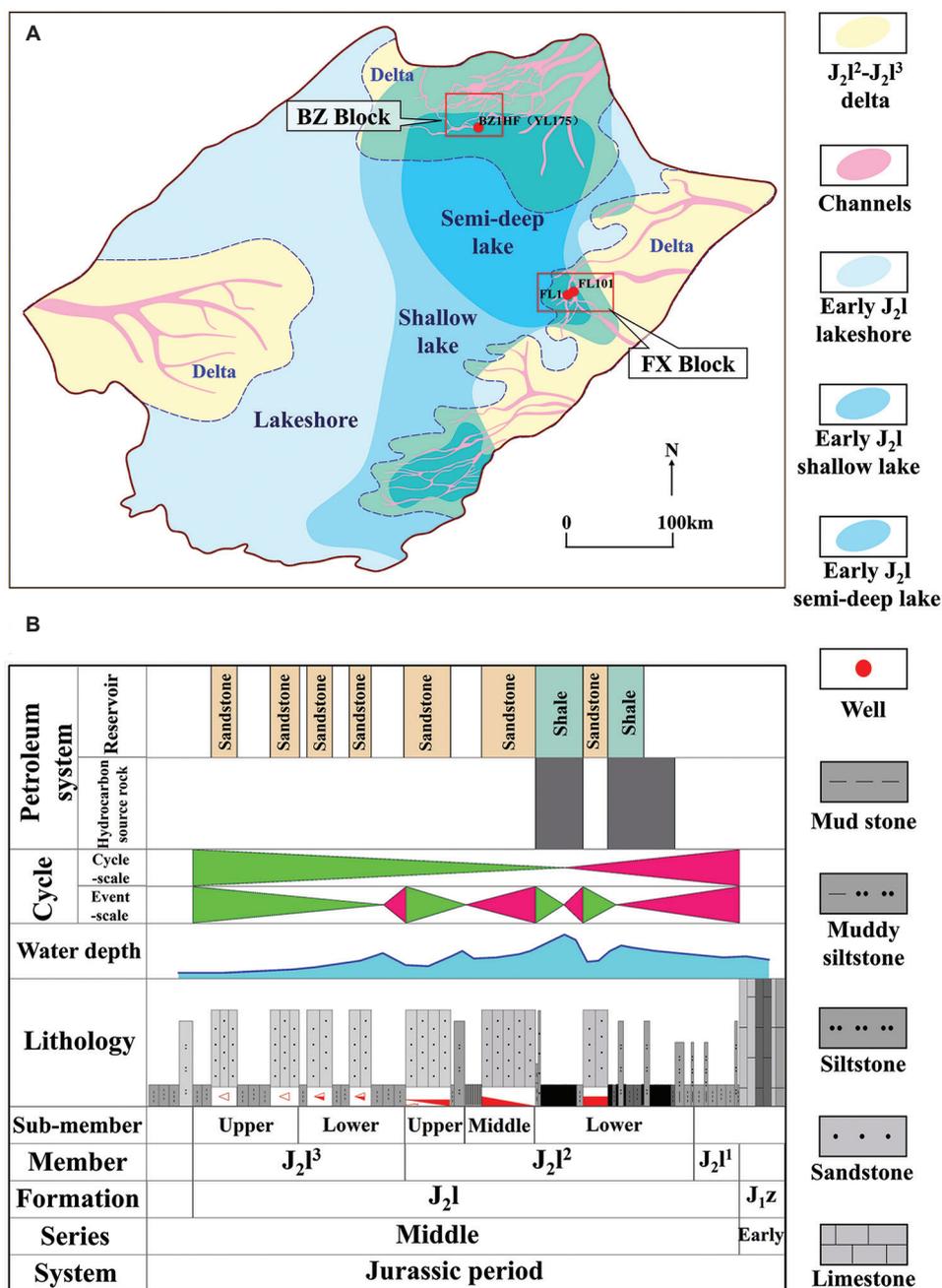
**Figure 1.** Hydrocarbon exploration and evaluation map of Lianggaoshan Formation, Sichuan Basin. (A) The hydrocarbon source rocks and channel overlay map from the Lianggaoshan Formation in the Sichuan Basin. (B) The lithostratigraphic column of the Jurassic system. Abbreviations: BZ: Bazhong; FX: Fuxing.

a high-fidelity elastic parameter model, significantly enhancing prediction accuracy both vertically and laterally.

### 3.1. AVO response analysis and attribute extraction

While post-stack seismic data provided a consolidated view by stacking pre-stack gathers across all incident angles, this process averages out critical AVO information, thereby masking lithological anomalies.[28] Pre-stack data analysis, however, leverages this very AVO information to delineate lithological changes and fluid effects, proving highly effective for identifying channel features.

This study leveraged AVO theory to characterize the seismic response of multi-phase channel sand
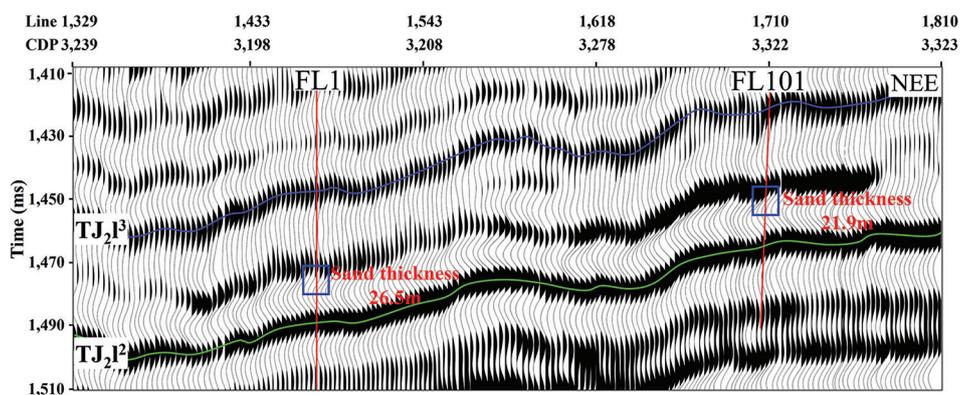
**Figure 2.** Post-stack seismic profile across Wells FL1 and FL101
Abbreviations: CDP: Common depth point; NEE: North-east-east direction.
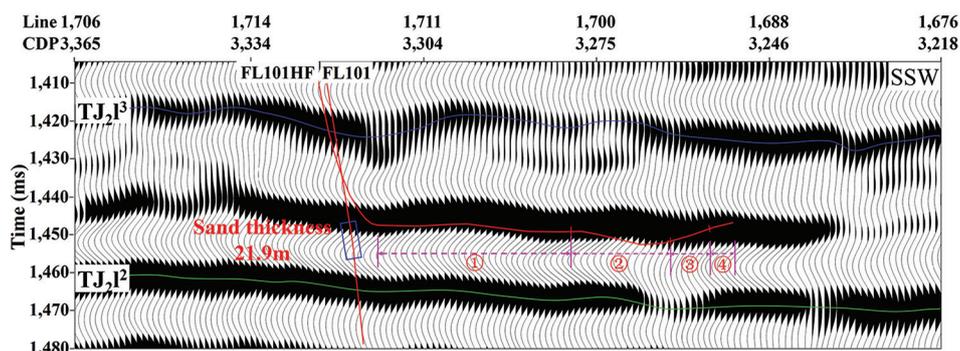


**Figure 3.** Post-stack seismic profile along the trajectory of Well FL101HF. ①, ②, ③, and ④ respectively represent the interval of sandstone, sand-mud interbedded, calcareous fine sandstone, and mudstone.
Abbreviations: CDP: Common depth point; SSW: South-south-west direction.

bodies encountered by horizontal well FL101HF. The well's trajectory intersected a sandstone interval, a sand-mud interbedded interval, and a calcareous fine sandstone interval before penetrating the overlying mudstone. A detailed analysis of pre-stack gathers at three representative common depth points (Table 1) revealed a common trend of amplitude reduction with increasing angle. The defining characteristic, however, is the markedly rapid amplitude decay in the sand-mud interbedded interval at far offsets (30–40°), creating a clear AVO response distinction from the other two intervals (Figure 4).

Based on the aforementioned AVO response analysis, this study demonstrated that AVO attributes can effectively reveal internal lithological variations within $J_2l^2$ channels. These attributes are typically extracted through fundamental pre-stack seismic inversion methods, which decode the implicit information in seismic data to characterize AVO anomaly variations.[29]

**Table 1. Forward modeling parameters table for the main lithological intervals encountered in the horizontal section of well FL101HF**

| Lithological intervals | P-wave velocity (m/s) | S-wave velocity (m/s) | Density (g/cm³) |
|---|---|---|---|
| Sandstone | | | |
| Mudstone | 4,834 | 2,685 | 2.610 |
| Sandstone | 5,424 | 3,191 | 2.640 |
| Sand-mud interbedded | | | |
| Mudstone | 4,834 | 2,685 | 2.610 |
| Mudstone | 5,022 | 2,870 | 2.564 |
| Calcareous fine sandstone | | | |
| Mudstone | 4,834 | 2,685 | 2.610 |
| Calcareous fine sandstone | 5,531 | 3,253 | 2.654 |

Analysis of Figure 4 indicates that the channel sandstones in the $J_2l^2$ generally exhibited a Class I AVO
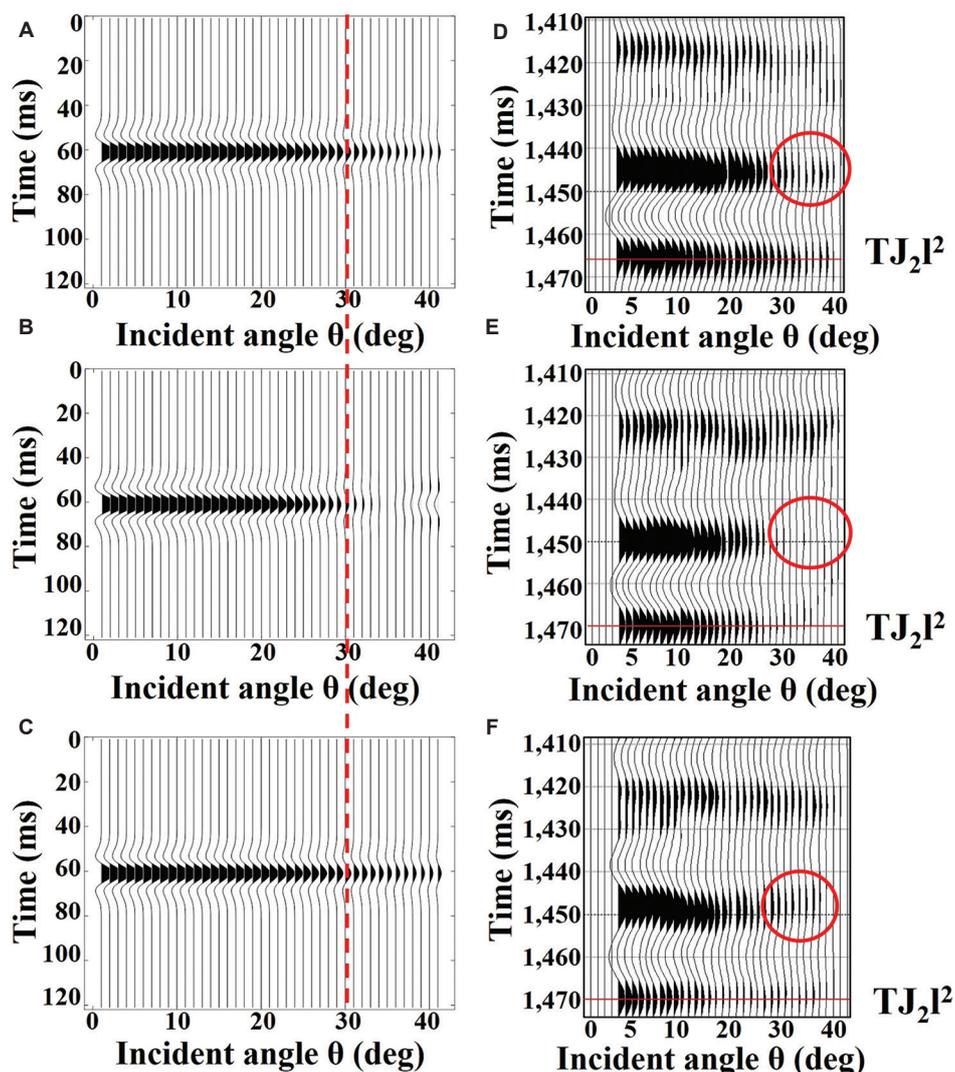
**Figure 4.** Comparison of (A-C) AVO forward modeling and (D-F) actual seismic gathers for different lithologies in Well FL101HF

response. Notably, within the 30–40° incident angle range, the sand-mud interbedded interval displayed significantly stronger amplitude variation with angle compared to other lithologies. Therefore, the gradient attribute was identified as the most sensitive parameter for highlighting intra-channel lithological variations.

### 3.2. AVO inversion method with GGD prior constraints

Conventional Bayesian inversion often employs the Gaussian distribution, the Laplace distribution, and the Huber distribution as priors. These prior constraints have relatively low precision and lack universality. To achieve a more accurate prediction of pre-stack elastic parameters, this study generalized the traditional Gaussian distribution

and constructed a GGD with stronger adaptability. The probability density function of its observed samples is as follows in **Equation 1**:

$$g\left(x;\alpha,\mu,\sigma\right)=\left[\frac{\alpha}{2\sigma\Gamma\left(\frac{1}{\alpha}\right)\sqrt{\Gamma\left(\frac{1}{\alpha}\right)\Big/\Gamma\left(\frac{3}{\alpha}\right)}}\right]e^{\left[-\left(\frac{|x-\mu|}{\sigma\sqrt{\Gamma\left(\frac{1}{\alpha}\right)\Big/\Gamma\left(\frac{3}{\alpha}\right)}}\right)^{\alpha}\right]}$$

$$(1)$$

where $\mu$ and $\sigma$ represent the mean and variance, respectively. $\alpha$ controls the shape of the probability density function and is defined as the degree of freedom of the GGD. The function $\Gamma\left(\bullet\right)$ satisfies $\Gamma\left(1/\alpha\right)=\int_{0}^{+\infty}e^{-x}x^{1/\alpha-1}\mathrm{d}x$.

The shape of the generalized Gaussian probability distribution is strongly influenced by the parameter $\alpha$: when the value of $\alpha$ is close to 0, the overall probability distribution values tend to be closer to the vicinity of the mean; when $\alpha = 1$, this probability distribution function is consistent with the Laplace probability distribution; when $\alpha = 2$, the shape of this probability distribution function is completely identical to that of the Gaussian probability distribution function; when $\alpha = +\infty$ (positive infinity), the probability distribution approximates a uniform distribution (Figure 5). Thus, the GGD can transition between several common probability distributions by adjusting the parameter $\alpha$, which unifies the common probability distribution functions to a certain extent and has stronger adaptability.

## 3.3. AVO inversion objective equation

Building on the analysis of AVO response characteristics and attribute extraction, this study further explored AVO inversion methods. Unlike post-stack inversion, pre-stack seismic inversion requires the use of angle information from pre-stack gathers and well logging data to conduct petrophysical crossplot analyses, aiming to obtain elastic parameters sensitive to lithology and reservoirs.[30,31] Recent studies have also demonstrated the effectiveness of pre-stack inversion based on the exact Zoeppritz equation for direct estimation of fluid properties and brittleness, which is crucial for predicting the sweet spot in unconventional reservoirs.[32]

### 3.3.1. AVO forward modeling equation

To fully utilize the amplitude information across all incident angles in pre-stack gathers, this study employed the exact Zoeppritz equation to generate synthetic gathers in the pre-stack, full-angle domain, thereby comprehensively capturing the AVO characteristics.[33] The expression is given in **Equation 2**:[34]

$$
\begin{bmatrix}
\sin\theta_1 & \cos\theta_3 & \sin\theta_2 & \cos\theta_4 \\
\cos\theta_1 & \sin\theta_3 & \cos\theta_2 & \sin\theta_4 \\
\sin 2\theta_1 & \dfrac{V_{P1}}{V_{S1}}\cos 2\theta_2 & \dfrac{V_{P1}V_{S2}^2\rho_2}{V_{P2}V_{S1}^2\rho_1}\sin 2\theta_2 & -\dfrac{V_{P1}V_{S2}\rho_2}{V_{S1}^2\rho_1}\cos 2\theta_4 \\
\cos 2\theta_3 & -\dfrac{V_{S1}}{V_{P1}}\sin 2\theta_3 & -\dfrac{V_{P2}\rho_2}{V_{P1}\rho_1}\cos 2\theta_2 & -\dfrac{V_{S2}\rho_2}{V_{P1}\rho_1}\sin 2\theta_4
\end{bmatrix}
$$
$$
\begin{bmatrix}
\mathbf{R}_{PP} \\ \mathbf{R}_{PS} \\ \mathbf{T}_{PP} \\ \mathbf{T}_{PS}
\end{bmatrix}
=
\begin{bmatrix}
\sin\theta_1 \\ \cos\theta_1 \\ \sin 2\theta_1 \\ -\cos 2\theta_3
\end{bmatrix}
\tag{2}
$$

The angles $\theta_1, \theta_2, \theta_3$, and $\theta_4$ correspond to the P-wave reflection, P-wave transmission, S-wave reflection, and S-wave transmission angles, respectively. These angles
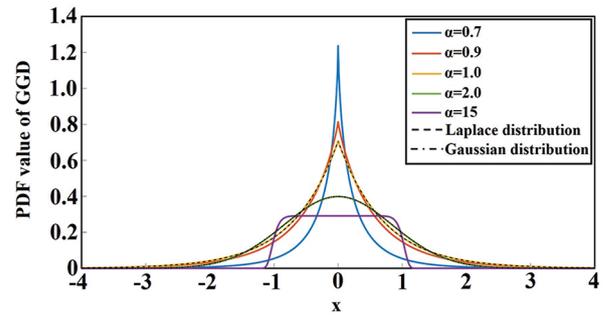


**Figure 5.** Probability density plot of the generalized Gaussian distribution
Abbreviation: GGD: Generalized Gaussian distribution.

satisfy Snell's law in relation to the P-wave and S-wave velocities of the medium. The upper and lower layers are characterized by P-wave velocities $V_{P1}$ and $V_{P2}$, S-wave velocities $V_{S1}$ and $V_{S2}$, and densities $\rho_1$ and $\rho_2$, respectively. The terms $R$ and $T$ denote reflection and transmission coefficients, with subscripts $PP$ and $PS$ indicating P-wave and converted-wave (S-wave) components, respectively.

Following generalized linear inversion theory, the P-wave reflection coefficient $R_{PP}$ in **Equation 2** was expanded using a first-order Taylor series approximation, yielding the linearized expression in **Equation 3**:

$$
\mathbf{R}_{PP} = \mathbf{R}_{PP}^{Int} + \frac{\partial \mathbf{R}_{PP}^{Int}}{\partial \mathbf{R}_{VP}}\Delta\mathbf{R}_{VP} + \frac{\partial \mathbf{R}_{PP}^{Int}}{\partial \mathbf{R}_{VS}}\Delta\mathbf{R}_{VS} + \frac{\partial \mathbf{R}_{PP}^{Int}}{\partial \mathbf{R}_{D}}\Delta\mathbf{R}_{D}
\tag{3}
$$

Where $R_{PP}^{Int}$ is the reflection coefficient of the initial model parameters; the reflection coefficients of $V_P$, $V_S$, and $\rho$ correspond to $R_{VP}$, $R_{VS}$, and $R_D$ in the above formula, respectively.

By setting $\mathbf{m} = \begin{bmatrix} \mathbf{R}_{VP} & \mathbf{R}_{VS} & \mathbf{R}_D \end{bmatrix}^T$ and $\mathbf{L} = \begin{bmatrix} \dfrac{\partial \mathbf{R}_{PP}^{Int}}{\partial \mathbf{R}_{VP}} & \dfrac{\partial \mathbf{R}_{PP}^{Int}}{\partial \mathbf{R}_{VS}} & \dfrac{\partial \mathbf{R}_{PP}^{Int}}{\partial \mathbf{R}_D} \end{bmatrix}$, we can obtain the following formula (**Equation 4**):

$$
R_{PP} = Lm \tag{4}
$$

In addition, the seismic synthetic record $S$ can be expressed as the product of the wavelet matrix and the reflection coefficient matrix, shown in **Equation 5**:

$$
S = WR_{PP} \tag{5}
$$

### 3.3.2. Inversion objective function

According to Bayes' theorem, the model parameters $m$ and the observed seismic data $D$ satisfy the following statistical law:[35]

$$
P(\mathbf{m}|\mathbf{D}) = \frac{P(\mathbf{D}|\mathbf{m})P(\mathbf{m})}{P(\mathbf{D})} \propto P(\mathbf{D}|\mathbf{m})P(\mathbf{m}) \tag{6}
$$

Among them, $P(m)$ is the marginal probability distribution of the actual data, which is generally assumed

to be a constant; therefore, the integral of the posterior probability distribution function P(m|D) equals 1. In general, it is assumed that the noise in seismic data follows a Gaussian distribution, and $P(D|M)$ as the likelihood function of model parameters and observed data, can be written as:

$$P(\mathbf{D}|\mathbf{m}) = \frac{1}{\left[(2\pi)^N \mathbf{C_d}\right]^2} e^{\left[-\frac{1}{2}(\mathbf{D}-\mathbf{Gm})^T \mathbf{C_d^{-1}}(\mathbf{D}-\mathbf{Gm})\right]} \tag{7}$$

In **Equation 7**, $\mathbf{C_d}$ is the covariance matrix of error data between synthetic records and observed data, $N$ is the number of time samples of the observed records, and G = WL. If we follow a GGD, $P(m)$ can be written as:

$$P(\mathbf{m}) = k_1 e^{\left[-\left(\frac{|\mathbf{m}|}{k_2}\right)^\alpha\right]} \tag{8}$$

In **Equation 8**,

$$k_1 = \frac{\alpha}{2\sigma\Gamma\left(\frac{1}{\alpha}\right)\sqrt{\Gamma\left(\frac{1}{\alpha}\right)/\Gamma\left(\frac{3}{\alpha}\right)}} \tag{9}$$

$$k_2 = \sigma\sqrt{\Gamma\left(\frac{1}{\alpha}\right)/\Gamma\left(\frac{3}{\alpha}\right)} \tag{10}$$

In general, when $\alpha$ is a fixed value, and $k_1$, $k_2$ are constants, the posterior probability density can be obtained as **Equation 11**:

$$P(\mathbf{D}|\mathbf{m}) = \frac{1}{\left[(2\pi)^N \mathbf{C_d}\right]^2} e^{\left[-\frac{1}{2}(\mathbf{D}-\mathbf{Gm})^T \mathbf{C_d^{-1}}(\mathbf{D}-\mathbf{Gm})\right]} \times k_1 e^{\left[-\left(\frac{|\mathbf{m}|}{k_2}\right)^\alpha\right]} \tag{11}$$

By omitting the constant terms in the above formula and calculating the maximum a posteriori solution of the model parameters, the following objective function (**Equation 12**) was constructed:

$$J_\sigma(m) = \frac{1}{2}(\mathbf{D}-\mathbf{Gm})^T(\mathbf{D}-\mathbf{Gm}) + \lambda(|\mathbf{m}|)^\alpha \tag{12}$$

In **Equation 12**, $\lambda = \mathbf{C_d}/k_2^\alpha$ is related to the degrees of freedom and the background noise of seismic signals.

To further improve the inversion accuracy of the model parameters in **Equation 12**, this study added a background constraint term to the equation. The new objective function is as follows in **Equation 13**:

$$J(m) = J_\alpha(m) + \beta(\mathbf{m}-\mathbf{m_{ref}})^T(\mathbf{m}-\mathbf{m_{ref}}) \tag{13}$$

Where, $\mathbf{m_{ref}}$ is the background trend of model parameters, which can be obtained from existing logging data or geological knowledge, and $\beta$ is the regularization parameter for this constraint term.

### 3.3.3. Algorithms for solving the objective function

**Equation 13** contains multiple regularization constraint terms and can be solved using the Alternating Direction Method of Multipliers.[36] First, the equation is decomposed into a subproblem $J_1(m)$ as follows in **Equation 14**,

$$J_1(\mathbf{m}) = \min_m\left[\frac{1}{2}\|\mathbf{D}-\mathbf{Gm}\|_2^2 + \lambda|\mathbf{m}|^\alpha\right] \tag{14}$$

and subproblem $J_2(m)$ as follows in **Equation 15**:

$$J_2(\mathbf{m}) = \frac{1}{2}\|\mathbf{D}-\mathbf{Gm}\|_2^2 + \beta\|\mathbf{m}-\mathbf{m_{ref}}\|_2^2 \tag{15}$$

Finally, subproblem $J_1(m)$ and subproblem $J_2(m)$ can be solved by the soft-thresholding algorithm and least-squares inversion, respectively. The detailed process for solving the objective function is given in Appendix 1.

### 3.4. Testing of the model

To verify the applicability of the proposed method, we performed a statistical analysis on the probability distributions of the three model parameters to be inverted for Wells FL1 and FL101 within the study area, namely the reflectivity series of P-wave velocity, S-wave velocity, and density. The results indicated that all three types of distributions derived from these two wells were in high agreement with the GGD ($\alpha = 0.83$), as illustrated in Figure 6.

As illustrated in Figure 7, we conducted a single-well inversion test using Well FL101 as a case study. The inversion results, constrained by both the Gaussian distribution and the GGD, exhibited a consistent overall trend. However, the GGD-constrained inversion demonstrated superior performance, with its P-wave and S-wave velocity results showing a higher degree of consistency with the original well log curves. Although both methods produced noticeable errors in density estimation, the GGD-derived density was more stable and aligned more closely with the actual well values. Consequently, the single-well test confirmed that the GGD-based inversion of the $J_2 l^2$ target interval achieved satisfactory consistency with the drilling data, meeting the accuracy prerequisites for subsequent channel sandstone prediction.

While the proposed pre-stack seismic inversion method theoretically enhances vertical resolution and stability—a benefit supported by single-well test results—it remains challenging to apply directly to three-dimensional volume prediction. Relying solely on high-frequency well information to build an interpolation model and extrapolating it laterally to form a low-
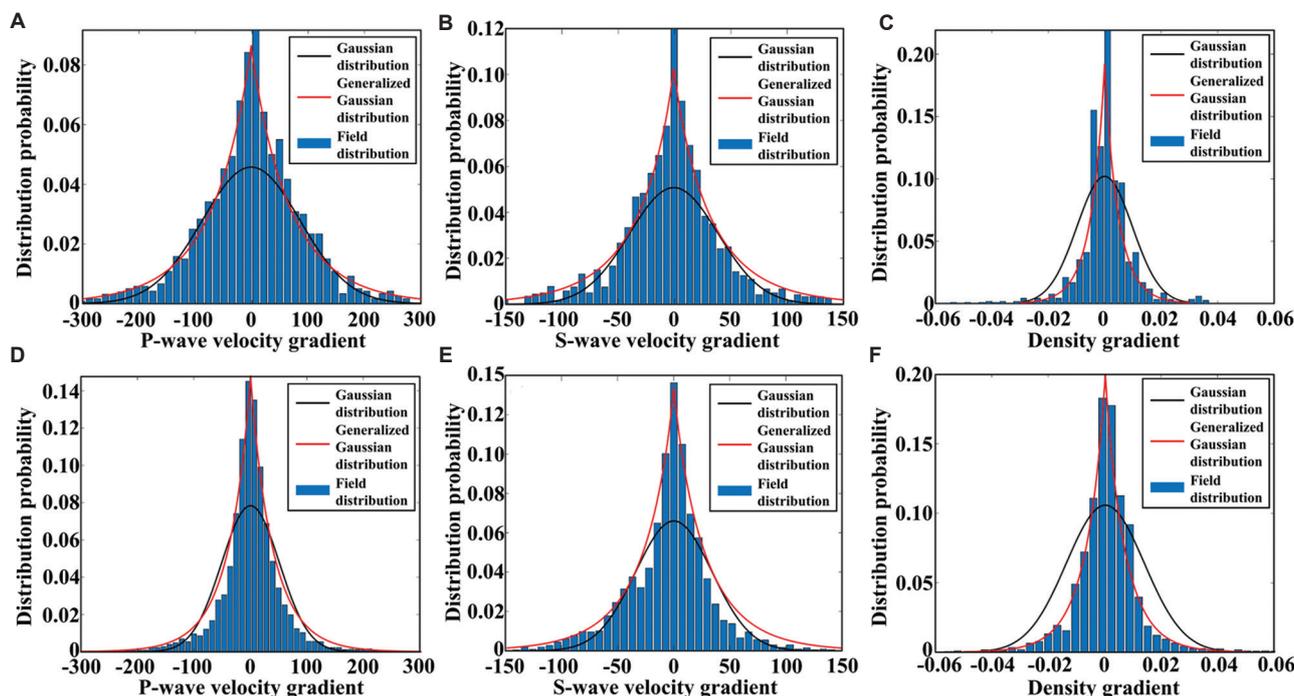
**Figure 6.** Probability distribution map (P-wave velocity, S-wave velocity, and density) from actual drilled wells to be inverted in (A-C) Wells FL101 and (D-F) FL1
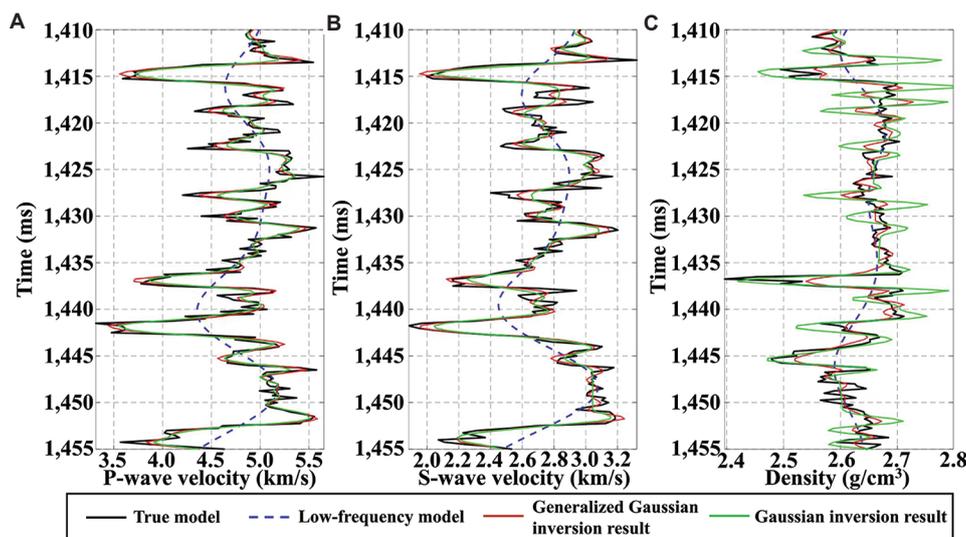


**Figure 7.** Comparison chart of inversion results and original curves for the target interval of the $J_2l^2$ in Well FL101. (A) P-wave velocity (km/s), (B) S-wave velocity (km/s), and (C) density (g/cm³).

frequency model often leads to significant discrepancies with actual seismic lateral variations. This approach tends to overemphasize well control and vertical resolution, resulting in strongly model-driven outcomes that compromise the accuracy of lateral geological anomaly resolution and obscure the spatial outlines of such anomalies.

For the complex $J_2l^2$ channels in the Fuxing Block, reference to existing studies confirms that inversion based exclusively on well data is inadequate for reliable characterization of these channels. Taking the P-wave velocity as an example, since the initial model constructed by means of well interpolation in the early stage yielded poor prediction results after extrapolation inversion and

exhibited low lateral resolution, the inversion results of the $J_2l^2$ channel in the lateral direction exhibited a model-driven effect, and the consistency with seismic waveforms was low. Thus, incorporating lateral resolution as a constraint is essential, though it remains a major challenge in conventional well-driven workflows.[37-41] As established earlier, the AVO gradient attribute effectively reflects intra-channel lithological changes. To improve lateral prediction accuracy, we constructed a low-frequency facies-controlled model by fusing the well-interpolated initial model with AVO gradient attributes in the frequency domain, using differentiated weights to construct a low-frequency facies-controlled model for inversion calculations. This approach

aims to balance the vertical and lateral resolution of the prediction results as much as possible. After a series of experiments (Figure 8), it was found that when the fusion weight of the well-interpolated initial model reaches or exceeds 50%—on the premise that a certain proportion of AVO attribute weight is incorporated—the inversion results can not only well delineate the distribution of channel sandstones in $J_2l^2$, but also identify the thin sand bodies developed in the upper strata of the $J_2l^2$ around the Well FL101.

Based on the above analysis, this study explored and summarized that the implementation of the low-frequency facies-controlled model mainly consists of two
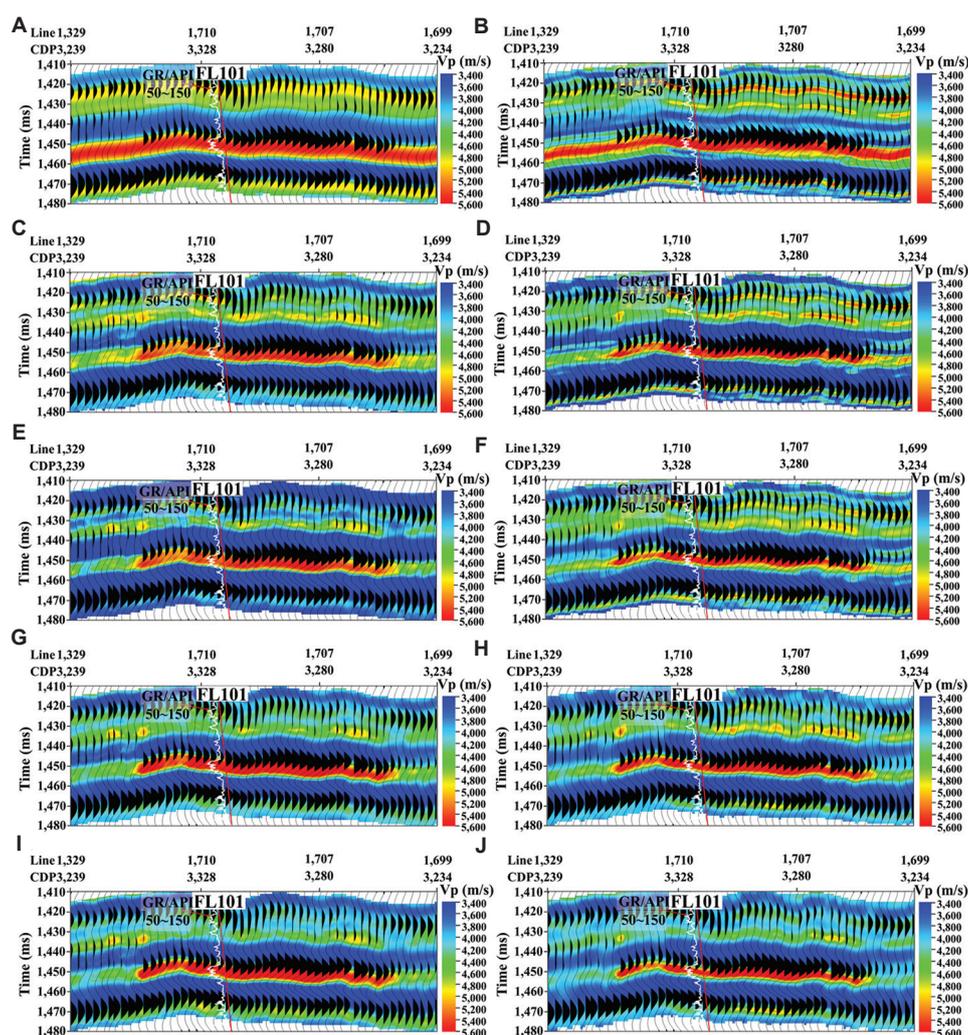


**Figure 8.** Fusion effects of the well-interpolated initial P-velocity (Vp) model and AVO gradient attributes under different weights, and their corresponding inversion results. (A and B) The initial model from a well-interpolated model, and its inversion results. (C and D) Fusion model with 60% weight of the well-interpolated model and 40% weight of the AVO gradient attributes, and its inversion results. (E and F) Fusion model with 50% weight of the well-interpolated model and 50% weight of the AVO gradient attributes, and its inversion results. (G and H) Fusion model with 40% weight of the well-interpolated model and 60% weight of the AVO gradient attributes, and its inversion results. (I and J) Initial model from AVO gradient attributes, and its inversion results.

Abbreviations: AVO: Amplitude versus offset; CDP: Common depth point; Vp: P-wave velocity.

key steps: first, normalizing the AVO attributes according to the value range of relevant elastic parameters; second, fusing the normalized attributes with the inter-well interpolation model. This operation ensured that the low-frequency facies-controlled model could preserve the lateral variation trend of AVO attributes during spatial extrapolation. When applied to subsequent inversion iterations, the model effectively balanced the vertical and lateral resolution of the inversion results. Taking P-wave velocity as an example, Figure 9 separately displays the inter-well interpolation model, AVO attributes, and the fused low-frequency facies-controlled model derived from their integration.

## 4. Application examples

### 4.1. Application result of Well FL101HF

Pre-stack AVO analysis of Well FL101HF identified the 30–40° incident angle range as the optimal window for detecting lithological variations within the horizontal section. By applying far-offset partial stacking within this range, internal response variations of the single bright-spot channel in the $J_2l^2$ were effectively enhanced. As demonstrated in Figure 10, the far-offset stacked section showed significantly attenuated amplitudes in sand-shale interbedded intervals, whereas sandstone and calcareous fine sandstone intervals maintained strong bright-spot
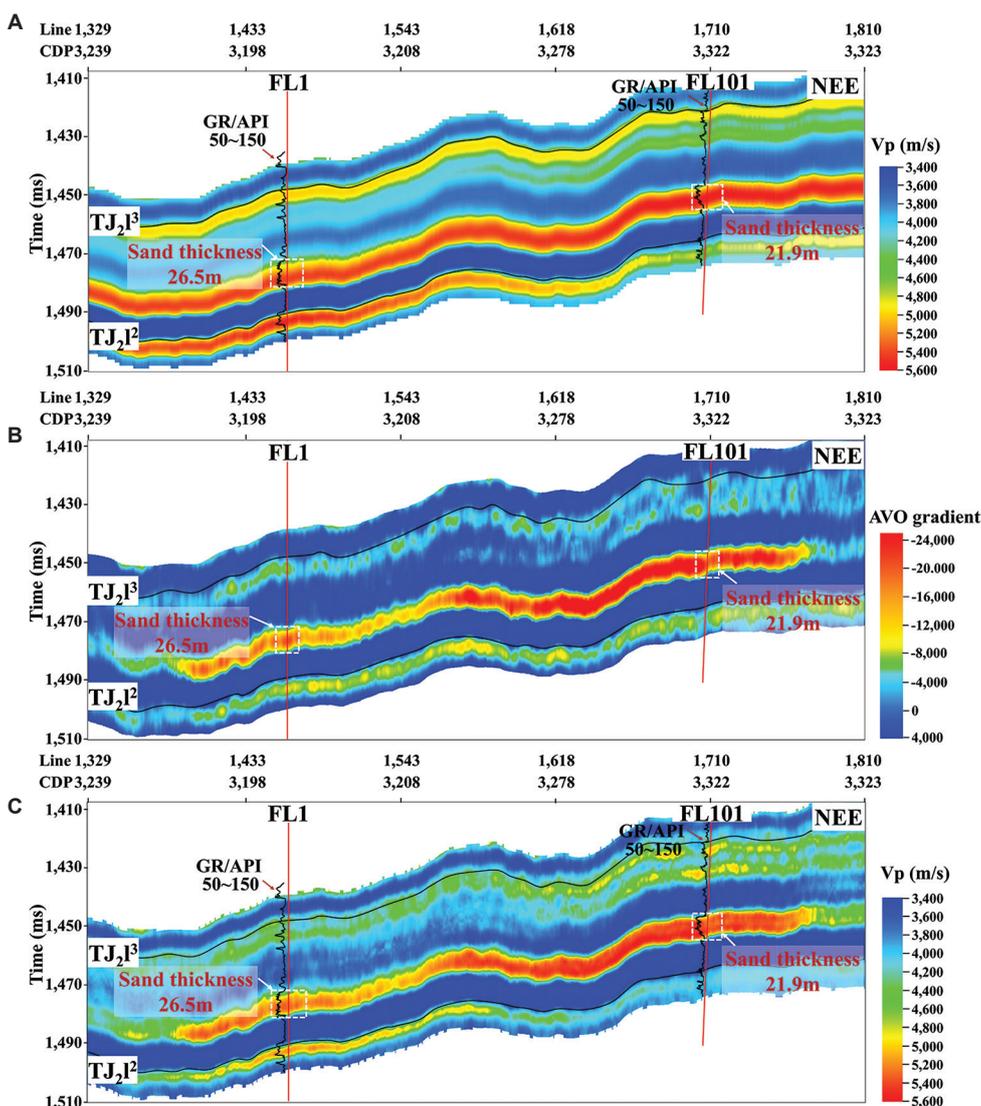


**Figure 9.** Cross-well profile through Wells FL1 and FL101. (A) Inter-well interpolation model of P-wave velocity. (B) AVO gradient attribute. (C) Facies-controlled model fused from an inter-well interpolation model and AVO attributes.
Abbreviations: AVO: Amplitude versus offset; CDP: Common depth point; NEE: North-east-east direction.

reflections. This result is consistent with actual drilling data and provides a more accurate lithological representation than conventional post-stack seismic data.

The observed amplitude variations confirm that lateral lithological changes produce distinct AVO responses, primarily manifested as differential rates of amplitude change with incident angle (gradient) across lithological units. This demonstrates that partial stacking effectively suppresses the dominant influence of small-to-medium angle amplitudes inherent in full-stack data, thereby accentuating the diagnostic amplitude characteristics of channel bright-spot reflections.

Based on the far-offset stacked seismic data (incident angle range: 30–40°), we conducted an isochronous slice analysis of bright-spot reflection characteristics using along-layer slicing. The advantage of along-layer slicing lies in its ability to extract the seismic response characteristics of specific phases of channels through horizon tracking and interpretation, thereby accurately delineating the distribution variation patterns of the sedimentary facies within the same-stage channels (Figure 11A). This effectively avoids the diachronism issue that arises when horizon-based slices are extracted using conventional isochronous framework models (Figure 11B). The results
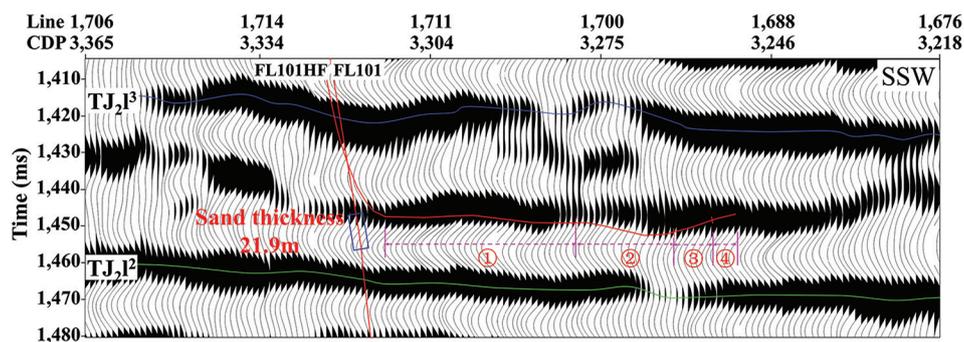


**Figure 10.** Far-offset (from 30° to 40°) stacked seismic profile through Well FL101HF. ①, ②, ③, and ④ respectively represent the interval of sandstone, sand-mud interbedded, calcareous fine sandstone, and mudstone, respectively.
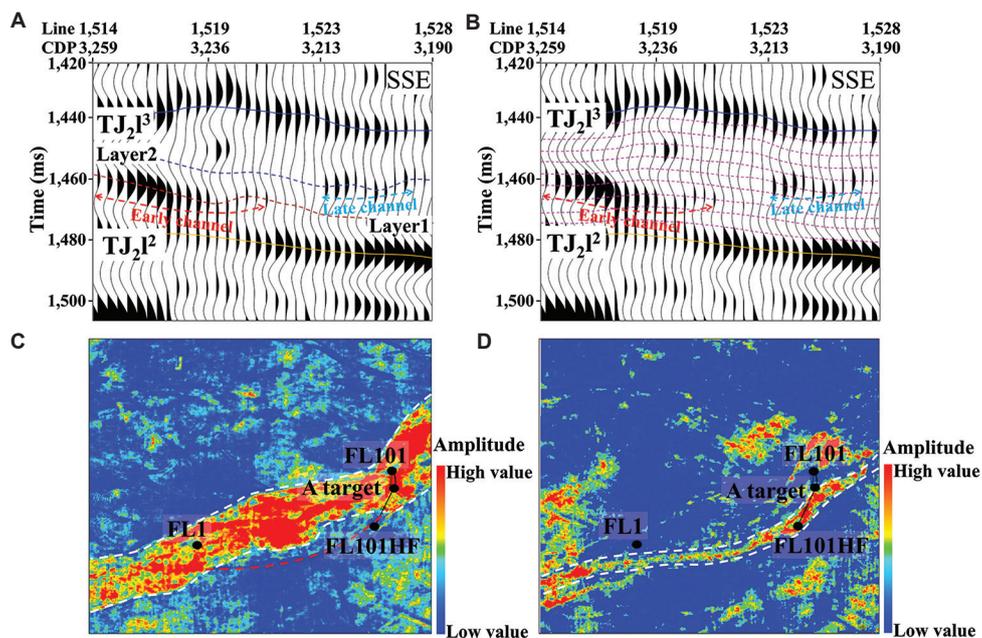Abbreviations: CDP: Common depth point; SSW: South-south-west direction.



**Figure 11.** Seismic profiles perpendicular to channels and amplitude of channels using along-layer slicing around Well FL101HF. (A) Along-layer slicing based on the horizon tracking method. (B) Along-layer slicing from an isochronous framework model. (C) Early-channel slice and (D) late-channel slice around Well FL101, which are based on the far-offset stacked seismic data.
Abbreviation: CDP: Common depth point.

indicate that the horizontal section of Well FL101HF penetrated two phases of superimposed channels (Figure 11C and D), resulting in a sand-shale interbedded lithology, which suggests a location near the channel margin. Specifically, the first half of the horizontal section primarily traversed early-stage channel deposits dominated by fine sandstone, whereas the latter half encountered late-stage channel facies characterized by calcareous fine sandstone, influenced by progressive lateral channel migration. During the migration between the two channel phases, a transitional zone featuring sand-shale interbedding developed along their margins.

Based on the GGD-constrained pre-stack inversion approach and the low-frequency facies-controlled modeling strategy, this study performed inversion tests in the Well FL101 area of the Fuxing Block. Petrophysical crossplot analysis confirms Young's modulus as a sensitive discriminator for channel sandstones in the Lianggaoshan Formation, with sandstone intervals exhibiting significantly higher values than mudstone intervals (Figure 12). This distinct contrast enables effective lithology differentiation within the $J_2l^2$ member. For the inversion process, an inter-well interpolation model derived from Wells FL1 and FL101 was integrated with AVO gradient attributes to construct a low-frequency facies-controlled model, providing essential geological constraints for the pre-stack seismic inversion.

Given the complex lithological conditions encountered by Well FL101HF in the $J_2l^2$ formation, Young's modulus was selected as the key lithology-sensitive parameter for pre-stack seismic inversion to validate prediction effectiveness. To verify the inversion performance of the proposed method, we compared its prediction results with those derived from the conventional pre-stack inversion method. Specifically, the prediction results of the conventional pre-stack inversion method (constrained by the Gaussian prior distribution) were generated using Conver (version 3.1.0.1), a professional geophysical
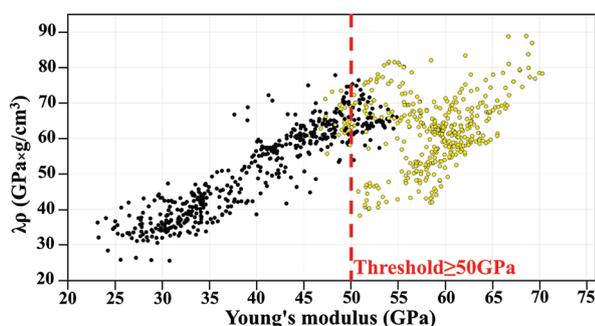
data processing software.[26] The prediction results of the conventional pre-stack inversion method exhibited relatively high Young's modulus values in the sand-mud interbedded intervals (Figure 13A), which are inconsistent with the actual drilling data (Figure 13C). Consequently, the lateral lithological variations in the horizontal section were not accurately characterized. Comparison with conventional pre-stack inversion results confirmed that the proposed method achieved superior consistency with actual drilling data (Figure 13B): sandstone intervals exhibited high Young's modulus values, while mudstone sections showed significantly lower values. Sand-mud interbedded intervals displayed characteristic alternating high-low modulus responses, and calcareous fine sandstone intervals showed markedly elevated modulus values. As the well trajectory exited the channel and entered the overlying mudstone near the bottom, Young's modulus decreased substantially. The prediction results demonstrate that the proposed method yielded markedly higher prediction accuracy for both vertical and lateral lithological variations.

Exploration results indicate that the $J_2l^2$ in the Fuxing Block contains delta-front subaqueous distributary channel sands, representing favorable reservoir facies. Within these main channels, sand bodies displayed vertical multi-phase superposition and lateral avulsion and migration patterns. The channel prediction plan derived from pre-stack inversion results (Figure 14) revealed multiple overlapping and migrating channel branches, with enhanced migration complexity in high-sinuosity segments. This confirms significant heterogeneity in sand body distribution, though stable sand development segments within main channels remain optimal targets for horizontal drilling.

Following segmented fracturing, a production test in Well FL101HF yielded an oil flow rate of 26.88 m³/d, demonstrating the substantial exploration potential of channel sandstones in the Jurassic Lianggaoshan Formation of the Sichuan Basin.

### 4.2. Promotion effect in Bazhong Block

Following the successful application in the Fuxing Block, the methodology was extended to the Bazhong Block. Geological evaluation confirmed the development of large-scale channel systems in the Jurassic $J_2l^2$ member of this region. Building on the exploration insights gained from the Fuxing Block and based on the stacking patterns of intra-channel sand bodies, the channel sedimentary models in the Bazhong Block were categorized into three distinct types: isolated, migratory, and superimposed. These classifications reflect the inherent heterogeneity within the channel complexes. Among these, the superimposed
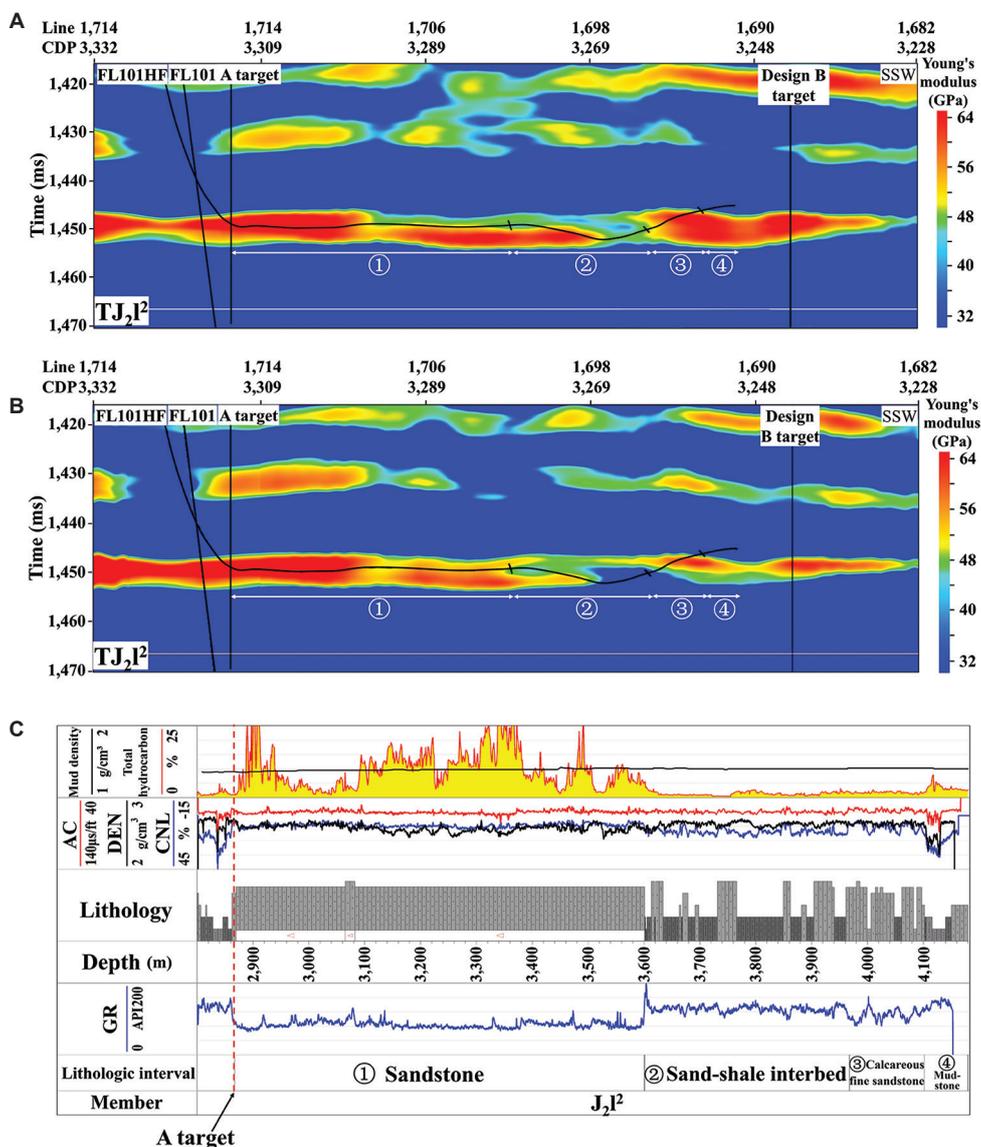


**Figure 12.** Crossplot of Young's modulus vs. lambda-rho in the second member of the Fuxing Block

**Figure 13.** Pre-stack inversion prediction profile through Well FL101HF. (A) Gaussian distribution prior constraint method. (B) Generalized Gaussian prior constraint inversion method. (C) Comprehensive histogram of Well FL101HF.
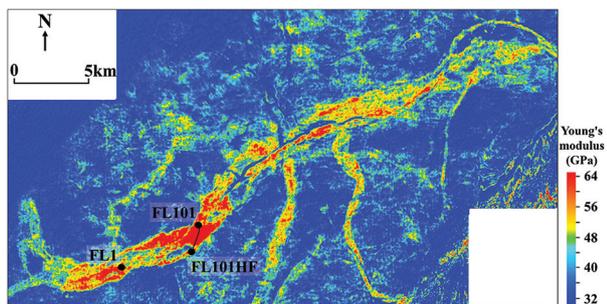Abbreviations: CDP: Common depth point; SSW: South-south-west direction.



**Figure 14.** Channel prediction plan of the second member of the Fuxing Block

type—characterized by thick, large-scale sand bodies— was identified as the most favorable exploration target (Figure 15).

To assess the exploration potential of tight sandstone channels in the Bazhong Block's Lianggaoshan Formation, a horizontal well was sidetracked from the original Well YL175. Drilling results confirmed complex lithological variations in the horizontal section, demonstrating significant vertical and lateral heterogeneity within the $J_2l^2$ channels. For detailed analysis, AVO gradient attributes were extracted to characterize internal channel architecture.

As shown in Figure 16, these attributes revealed substantial heterogeneity across the study area.

Given the strong trough-bright-spot characteristics exhibited by $J_2l^2$ channel sandstones in post-stack seismic data, reversed-polarity seismic profiles were compared with AVO attributes to delineate lateral sand body superposition relationships. Well YL175, positioned in the southern straight segment of the channel system, encountered 25-meter-thick sandstones interpreted as the superimposed type based on AVO gradient attributes (Figure 16A). North of this segment, the channel morphology was more sinuous, exhibiting clear evidence of lateral migration in the curved sections (Figure 16C). Cross-sectional views perpendicular to these curved



**Figure 15.** Main sedimentary models of channels from the second member of the Bazhong Block. (A) Isolated type, (B) migratory type, and (C) superimposed type.

segments consistently displayed migratory patterns in AVO gradient attributes, confirming the coexistence of multiple sand body superposition patterns within the channel system near Well YL175.

Well BZ1HF, a horizontal well drilled from the YL175 platform, encountered similarly complex lithological conditions in its horizontal section as those observed in Well FL101HF from the Fuxing Block, primarily resulting from dynamic variations in the well trajectory (Figure 17A). In this study, the P-wave velocity/S-wave velocity (Vp/Vs) ratio was employed as a sensitive diagnostic parameter for distinguishing sandstone and mudstone lithologies. A low-frequency facies-controlled model, constructed using AVO gradient attributes, was utilized to constrain the pre-stack seismic inversion.

The inversion results demonstrated a strong correlation between the predicted Vp/Vs profile and the actual drilling data (Figure 17A): mudstone intervals were characterized by high Vp/Vs ratios, sandstone intervals by low ratios, and sand-shale interbeds exhibited intermediate values. The inversion-based plan view (Figure 17B) further confirms that Well BZ1HF is situated within the southern straight segment of the channel system, where laterally extensive, thick superimposed sand bodies—similar to those encountered in Well YL175—are well developed. These consistent results validate the effectiveness and reliability of the proposed pre-stack seismic prediction methodology.
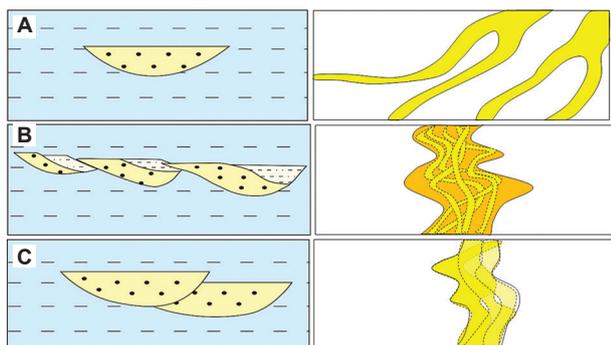


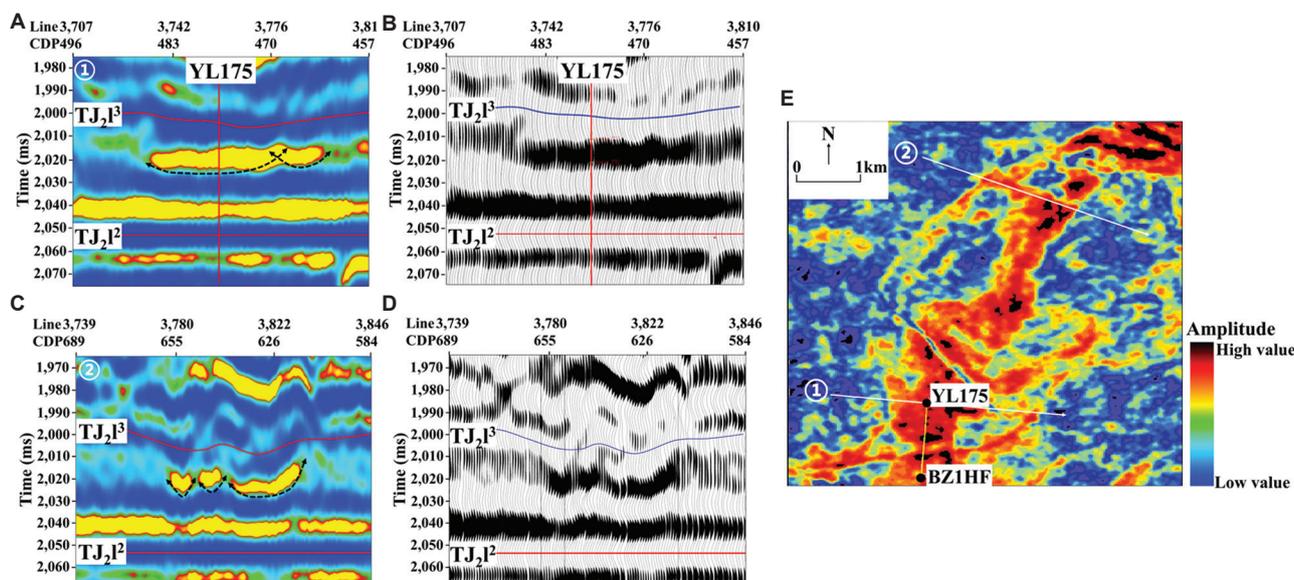**Figure 16.** AVO gradient attribute plane and profile of the second member in the Bazhong block. (A and B) AVO gradient attribute profile and anti-polar seismic profile of well YL175. (C and D) AVO gradient attribute profile and anti-polar seismic profile of channel north section of the second member. (E) AVO gradient attribute plane.
Abbreviations: AVO: Amplitude versus offset; CDP: Common depth point.
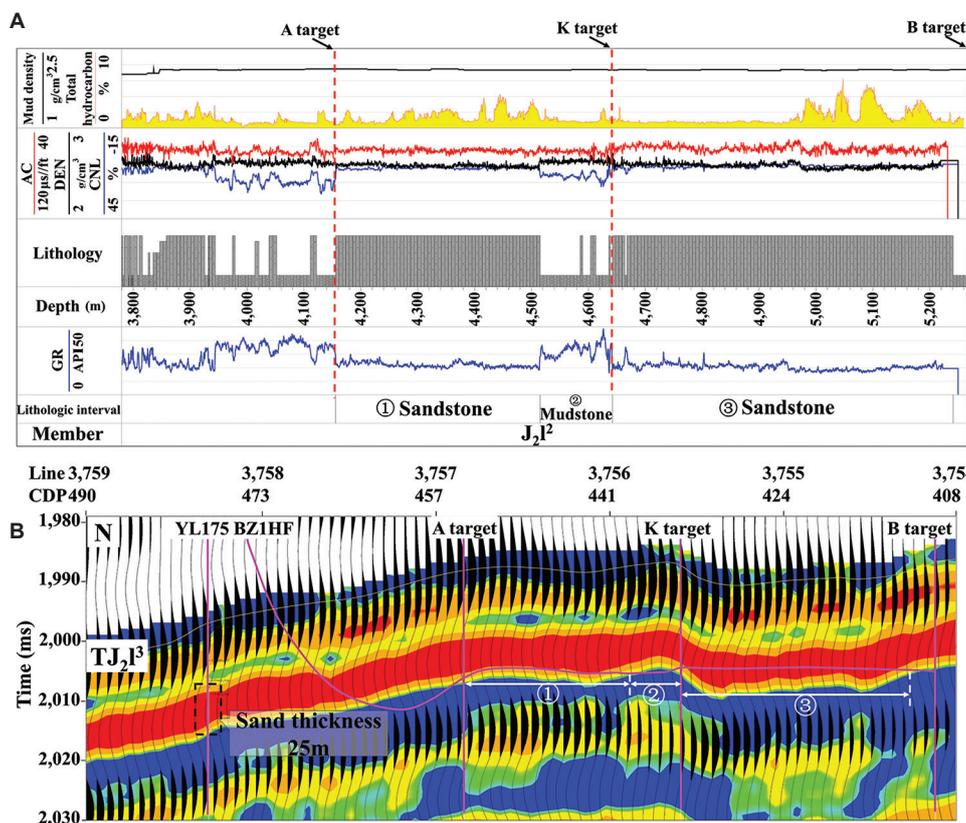
**Figure 17.** Comparison diagram of inversion and actual drilling results in the second member, through Well BZ1HF, Bazhong Block. (A) Comprehensive lithological histogram of Well BZ1HF. (B) Inversion prediction profile of P-wave/S-wave velocity (Vp/Vs) ratio through Well BZ1HF. Abbreviation: CDP: Common depth point.



**Figure 18.** Pre-stack inversion prediction map of second member channels, Bazhong Block. (A) Channel prediction plan. (B) Isolated type. (C) Migratory type. (D) Superimposed type.
Abbreviations: CDP: Common depth point; E: East direction; NEE: North-east-east direction; NNW: North-north-west direction; Vp/Vs: P-wave velocity/S-wave velocity.

Building on the inversion results, this study further investigated the spatial distribution characteristics of $J_2l^2$ channels across di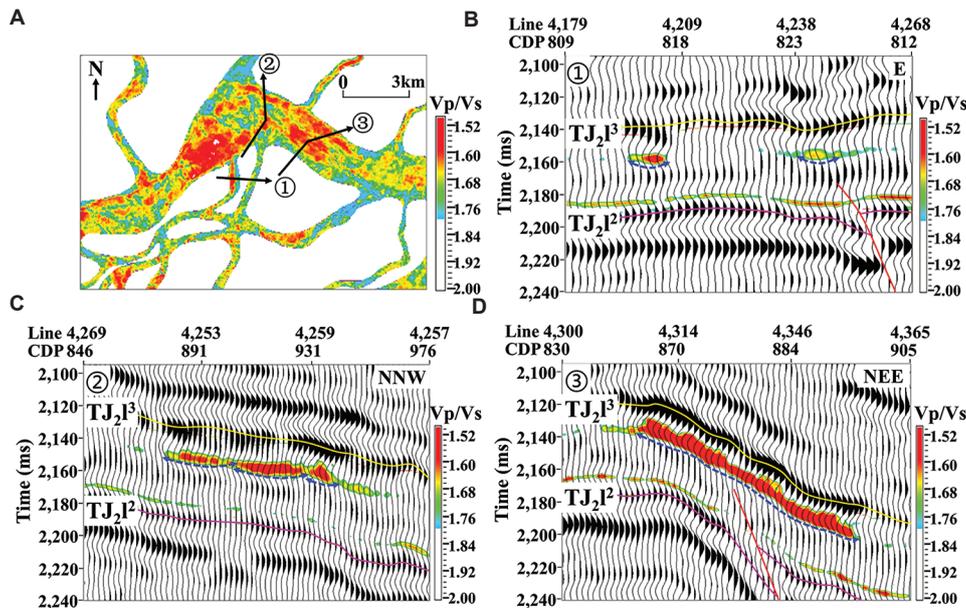fferent geomorphological segments. By applying the geological classification model established in Figure 15, three distinct channel types were analyzed: narrow, straight-wide, and high-sinuosity segments (Figure 18). The analysis revealed a systematic distribution pattern: isolated channel sand bodies of limited scale predominantly occurred in narrow segments; migratory sand bodies with strong lateral heterogeneity developed mainly in high-sinuosity segments; while thick, large-scale superimposed sand bodies characterized the straight-wide segments.

The production performance of Well BZ1HF, yielding 126.00 m³/d of oil and 57,700 m³/d of gas, confirmed that straight-wide segments represent the most favorable exploration targets. The methodology demonstrated in this study successfully captured the internal architectural complexity of $J_2l^2$ channels and provides reliable technical support for subsequent exploration and reservoir evaluation.

## 5. Conclusion

This study presents a pre-stack seismic workflow centered on GGD prior constraints to enhance the characterization of complex channel sandstones in the $J_2l^2$ member. Key findings demonstrated that pre-stack AVO analysis effectively identified an optimal incident angle range (30–40°), which, when applied through partial stacking, resolved the complex lithological heterogeneities encountered in Well FL101HF. Furthermore, AVO gradient attributes were established as a highly sensitive indicator for delineating lateral lithological variations within the channels, a finding validated across both the Fuxing and Bazhong Blocks. Integrating these AVO attributes with inter-well models to construct a low-frequency facies-controlled model significantly improved the lateral predictive capability of the subsequent GGD-constrained pre-stack inversion. This method provides a robust approach for fine-scale vertical and lateral prediction of complex channels, offering critical technical support for tight sandstone exploration and development.

## Acknowledgments

## Funding

## Conflict of interest

The authors declare no potential conflict of interest.

## Author contributions

*Conceptualization:* Meng Yuan
*Formal analysis:* Chang Sun
*Investigation:* Jianlong Su
*Methodology:* Zhiwei Miao
*Visualization:* Lei Pan
*Writing–original draft:* Meng Yuan
*Writing–review & editing:* Meng Yuan

## Availability of data

All data analyzed have been presented in the paper.

## References

1. Wu XY, Liu TY. Analysis of seismic spectral attenuation based on Wigner-Ville distribution for sandstone reservoir characterization-a case study from West Sichuan Depression, China. *J Seismic Explor*. 2010;19(1):69-85.

2. Zhang DW, Yang Y. Exploration potential and development direction of continental tight sandstone gas in the Sichuan basin. *Natural Gas Industry*. 2022;42(1):1-11.

   doi: 10.3787/j.issn.1000-0976.2022.01.001

3. Liu H, Lei X, Mao C, Li S. Improving reservoir thickness prediction using seismic attributes and attributes fusion. *Acta Geophysica*. 2014;62(3):544-563.

   doi: 10.2478/s11600-013-0174-5

4. Li QZ. Discussion on seismic exploration of lithologic reservoirs. *Litholgic Reserv*. 2008;20(2):45-54.

   doi: 10.3969/j.issn.1673-8926.2008.02.001

5. Li GF, Xiong JL, Zhou H, Zhai TL. Seismic reflection characteristics of fluvial sand and shale interbedded layers. *Appl Geophys*. 2008;5(3):219-229.

   doi: 10.1007/s11770-008-0025-3

6. Bi J, Gu H, Liu S, Guan X. Analysis on seismic response characteristics of channel sands and its influence factors: Case study of Upper Guantao Formation in KD1 area. *Geophys Prospect Petrol*. 2013;52(1): 97-103. [Article in Chinese].

   doi: 10.3969/j.issn.1000-1441.2013.01.015

7. Zhang X, Hu G, Fan T, Jing Y, Wang H, Yu B. Seismic response analysis and prediction for fluvial reservoir architecture. *China Offshore Oil Gas*. 2018;30(1):110-117. [Article in Chinese].

   doi: 10.11935/j.issn.1673-1506.2018.01.013

8. Li HH, Yue DL, Li W, Guo CC, Li X, Lyu M. Identification of point bar and abandoned channel of meandering river by spectral decomposition inversion based on machine learning. *Oil Geophys Prospect*. 2023;58(2):358-368.

   doi: 10.13810/j.cnki.issn.1000-7210.2023.02.013

9.   Zhang JL, Cheng BJ, Xu TJ, Yong L. Identification of paleochannels by seismic attribute principal component analysis. *Oil Geophys Prospect*. 2023;58(1):190-195.

doi: 10.13810/j.cnki.issn.1000-7210.2023.01.020

10.  Xu H, Du X, Gao J, *et al*. Quantitative interpretation of sedimentary microfacies based on waveform clustering: A case study of X oilfield, Middle East. *Geophys Prospect Petrol*. 2018;57(5):744-755. [Article in Chinese]

doi: 10.3969/j.issn.1000-1441.2018.05.014

11.  Lu M, Bai JH, Jiao YL, *et al*. A PCA and wavelet packet transform integrated method for high-precision identification of abandoned channels in large meandering river systems. *J Geophys Eng*. 2025;22(5):1392-1405.

doi: 10.1093/jge/gxaf082

12.  Qian YL, Hu QX, Wang XH, Wang KP, Shi QD. Application of seismic waveform indicator inversion in thin sandstone prediction technology. *J Chongqing Univ Sci Technol (Nat Sci Ed)*. 2017;19(6):17-20.

doi: 10.19406/j.cnki.cqkjxyxbzkb.2017.06.005

13.  Gui PJ, Gao ZP, Cao SH, Wen LF. Application of AVO based on pre-stack seismic data in subtle channel identification of Dongsheng gas field. *Petrol Geol Eng*. 2022;36(6):1-7.

doi: 10.3969/j.issn.1673-8217.2022.06.001

14.  Liu XY, Li MH, Ye TR. Fine characterization of complicated channels in Western Sichuan and identification of sedimentary facies. *Geophys Prospect Petrol*. 2019;58(05):750-757.

doi: 10.3969/j.issn.1000-1441.2019.05.014

15.  Sun ZT, Yin XY, Ji YZ. Angle-dependent seismic attenuation-based gas-bearing detection of a sandstone river channel reservoir in the western Sichuan basin. *J Geophys Eng*. 2024;21(3):913-921.

doi: 10.1093/jge/gxae042

16.  Sotelo V, Almanza O, Montes L. Post-stack seismic inversion through probabilistic neural networks and deep forward neural networks. *Earth Sci Inform*. 2024;17(3):1957-1966.

doi: 10.1007/s12145-024-01251-4

17.  Yang T, Wang PQ, Li QC, Huo KY, Li W, He XK. A pre-stack nonlinear inversion method for joint PP-PS wave based on exact Zoeppritz equation. *Oil Geophys Prospect*. 2025;60(1):152-203.

doi: 10.13810/j.cnki.issn.1000-7210.20240015

18.  Wang J, Wu YN, Wang T, Jia WL, Bao YF, Liu LF. Multi-level sparse regularization inversion method for seismic frequency division: A case study from the second member of paleogene dongying formation in shijiutuo uplift, bozhong sag. *Litholgic Res*. 2025;37(4):38-49.

doi: 10.12108/yxyqc.20250404

19.  Chen K, Dai JC, Wei W, *et al*. Lithofacies classification of tight sandstone based on bayesian facies-AVO attributes: A case study of the first member of jurassic shaximiao formation in central sichuan basin. *Litholgic Res*. 2024;36(5):111-121.

doi: 10.12108/yxyqc.20240511

20.  Yang WY, Wei XJ, Li HS. The past, present and future of intelligent geophysical technology. *Lithologic Res*. 2024;36(2):170-188.

doi: 10.12108/yxyqc.20240216

21.  Zhang SH, Liu YJ, Liu XH. Prediction technique of high-quality reservoir in tight reservoir of the sixth member of Xujiahe formation in Jiannan area. *Lithologic Reserv*. 2015;27(3):98-102.

doi: 10.3969/j.issn.1673-8926.2015.03.015

22.  Zhou ZQ. Simulation and prediction of tight sandstone reservoirs based on waveform facies-controlled inversion: A case study from the second member of Paleogene Kongdian Formation in Southern Cangdong sag. *Lithologic Reserv*. 2024;36(5):77-86.

doi: 10.12108/yxyqc.20240508

23.  Niu LP, Hu HF, Zhou D, Zheng XD, Geng JH. Bayesian prestack seismic stochastic inversion based on the exact Zoeppritz equation. *Geophys Geochem Explor*. 2024;48(1):77-87.

doi: 10.11720/wtyht.2024.2572

24.  Cao YM, Zhou H, Yu B, Zhang YG, Dai SL. Prestack seismic stochastic inversion method based on spatial co-simulation. *Oil Geophys Prospect*. 2024;59(2):268-278.

doi: 10.13810/j.cnki.issn.1000-7210.2024.02.009

25.  Wu S, Han B, Ji LX, Sun ZX. Pre-stack AVO inversion for estimating effective pressure in sandstone reservoirs. *Oil Geophys Prospect*. 2024;59(5):1165-1173.

doi: 10.13810/j.cnki.issn.1000-7210.2024.05.020

26.  Huang HD, Yuan S, Zhang Y, Zeng J, Mu W. Use of nonlinear chaos inversion in predicting deep thin lithologic hydrocarbon reservoirs: A case study from the Tazhong oil field of the Tarim Basin, China. *Geophysics*. 2016;81(6):B221-B234.

doi: 10.1190/geo2015-0705.1

27.  Yin XY, Zhou QC, Zong AY, Liu HQ. AVO inversion with t-distribution as priori constraint. *Geophys Prospect Petrol*. 2014;53(1):84-92.

doi: 10.3969/j.issn.1000-1441.2014.01.012

28.  Zhang J, Gao J, Wang L, Dong B, Cai Z, Cheng R. Study on multicomponent amplitude versus offset forward modelling of thin layer gas hydrate using the Brekhovskikh equation. *Geophys Prospect*. 2023;72(4):1350-1361.

doi: 10.1111/1365-2478.13375

29. Rutherford SR, Williams RH. Amplitude-versus-offset variations in gas sands. *Geophysics*. 1989;54(6):680.

doi: 10.1190/1.1442696

30. Chen X, Li S, Wei Z, Ning J, Yang X, Pre-stack seismic inversion based on one-dimensional GRU combined with two-dimensional improved ASPP. *J Geophys Eng*. 2024;21(6):1791-1809.

doi: 10.1093/jge/gxae106

31. Yang YM, Yin XY, Li K, Zhang F, Gao JH. Fast pre-stack multi-channel inversion constrained by seismic reflection features. *Petrol Sci*. 2023;20(4):2060-2074.

doi: 10.1016/j.petsci.2023.02.009

32. Zhang S, Huang HD, Dong YP, Yang X, Wang C, Luo YN. Direct estimation of the fluid properties and brittleness via elastic impedance inversion for predicting sweet spots and the fracturing area in the unconventional reservoir. *J Nat Gas Sci Eng*. 2017;45:415-427.

doi: 10.1016/j.jngse.2017.04.028

33. Wu S, Wang Y, Li Q, He Z, Geng J. Joint data-driven and physics-driven prestack amplitude-variation-with-angle elastic parameter inversion. *Geophysics*. 2024;89(1):R17-R32.

doi: 10.1190/geo2023-0135.1

34. Zuo Y, Zong Z, Li K, Luo K. Bayesian AVOAz inversion of fluid and anisotropy parameters using Gibbs sampling with AISM algorithm. *IEEE Trans Geosci Remote Sens*. 2024;62:1-15.

doi: 10.1109/tgrs.2024.3484435

35. Wang C, Yin X, Shi XW, Pan SL, Gou QY. Direct prediction method of fracturing ability in shale formations based on pre-stack seismic inversion. *J Seism Explor*. 2022;31(5):407-424.

36. Gao B, Ma F. Symmetric alternating direction method with indefinite proximal regularization for linearly constrained convex optimization. *J Optimiz Theor Applic*. 2017;176(1):178-204.

doi: 10.1007/s10957-017-1207-z

37. Zhang X, Li YW, Guan X, Long JY, Xiong Y. Research and application of pre-stack fast inversion technology based on lithology data reconstruction. *Oil Geophys Prospect*. 2024;59(5):1141-1154.

doi: 10.13810/j.cnki.issn.1000-7210.2024.05.018

38. She YW, Zhang MB, Wang YG, Zhang Y, Li F. Application of phase-controlled pre-stack inversion technique based on rock physics analysis in bauxite reservoir prediction: A case study of the Qingcheng district in the Ordos Basin. *Nat Gas Geosci*. 2024;35(8):1432-1440.

doi: 10.11764/j.issn.1672-1926.2024.05.001

39. Zhang S, Chang S, Huang H, *et al*. Prediction of favorable carbonate reservoirs under extremely thick salts via poststack facies-controlled and prestack zoeppritz equation inversions in the Santos basin of Brazil. *Geofluids*. 2020;2020(1):6205185.

doi: 10.1155/2020/6205185

40. Zhang S, Huang H, Zhu B, Li H, Zhang L. Seismic facies-controlled prestack simultaneous inversion of elastic and petrophysical parameters for favourable reservoir prediction. *Explor Geophys*. 2018;49(5):655-668.

doi: 10.1071/EG17048

41. Jia W, Zong Z, Lan T. Elastic impedance inversion incorporating fusion initial model and kernel Fisher discriminant analysis approach. *J Petrol Sci Eng*. 2023;220:111235.

doi: 10.1016/j.petrol.2022.111235

42. Lyu Q, Lin Z, She Y, Zhang C. A comparison of typical $\ell_p$ minimization algorithms. *Neurocomputing*. 2013;119:413-424.

doi: 10.1016/j.neucom.2013.03.017

## Appendix 1

### Appendix: Solution methods for Equation 13

**Equation 14** in the original manuscript is written in the vector form as follows:

$$J(\mathbf{m}) = \min_{\mathbf{m}} \left( \frac{1}{2} \|\mathbf{D} - \mathbf{Gm}\|_2^2 + \lambda \|\mathbf{Dm}\|_\alpha^\alpha + \beta \|\mathbf{m} - \mathbf{m}_{\text{ref}}\|_2^2 \right) \tag{A1}$$

A Lagrangian operator term was introduced into the above formula. H = Lm converts the above formula into an unconstrained optimization problem. The new formula is as follows:

$$J(\mathbf{m}) = \min_{\mathbf{m}} \left( \frac{1}{2} \|\mathbf{D} - \mathbf{Gm}\|_2^2 + \lambda \|\mathbf{H}\|_\alpha^\alpha + \beta \|\mathbf{m} - \mathbf{m}_{\text{ref}}\|_2^2 + \gamma \|\mathbf{H} - \mathbf{Lm}\|_2^2 - 2\gamma\mu^{\mathrm{T}}(\mathbf{H} - \mathbf{Lm}) \right) \tag{A2}$$

Here, $\gamma$ denotes the regularization parameter term of the Lagrange multiplier, and is the Lagrange multiplier corresponding to the constraint term in **Equation A2**. Based on the framework of the Alternating Direction Method of Multipliers, the objective function is decomposed into sub-functions related to m and H, respectively. Among them, the objective function associated with m is the same as **Equation 14** in the manuscript, which is expressed as follows:

$$J(\mathbf{m}) = \min_{\mathbf{m}} \left( \frac{1}{2} \|\mathbf{D} - \mathbf{Gm}\|_2^2 + \beta \|\mathbf{m} - \mathbf{m}_{\text{ref}}\|_2^2 + \gamma \|\mathbf{H} - \mathbf{Lm}\|_2^2 - 2\gamma\mu^{\mathrm{T}}(\mathbf{H} - \mathbf{Lm}) \right) \tag{A3}$$

**Equation A3** is a conventional optimization problem, and the update rule for m can be directly derived using the least squares method for solution using **Equation A4**:

$$\mathbf{m}^{i+1} = \left( \mathbf{G}^{\mathrm{T}}\mathbf{G} + \beta\mathbf{I} + \gamma\mathbf{L}^{\mathrm{T}}\mathbf{L} \right)^{-1} \left( \mathbf{G}^{\mathrm{T}}\mathbf{L} + \beta\mathbf{m}_{\text{ref}} + \gamma\mathbf{L}^{\mathrm{T}}\left( \mathbf{H}^i - \mu^i \right) \right) \tag{A4}$$

where I denotes the identity matrix. After obtaining the updated m, the sub-function in the following formula can be solved using **Equation A5**:

$$J(\mathbf{H}) = \min_{\mathbf{H}} \left( \lambda \|\mathbf{H}\|_\alpha^\alpha + \gamma \|\mathbf{H} - \mathbf{Lm}\|_2^2 - 2\gamma\mu^{\mathrm{T}}(\mathbf{H} - \mathbf{Lm}) \right) \tag{A5}$$

In **Equation A5**, the objective function is an optimization problem analogous to the one based on the Lp quasi-norm, and the soft-thresholding shrinkage algorithm is introduced herein for its solution:[42]

$$\mathbf{X}^{k+1} = \mathbf{Lm}^{i+1} + \mu^i \tag{A6}$$

By substituting **Equation A6** into **Equation A5**, we can obtain

$$\mathbf{H}^{i+1} = \operatorname*{argmin}_{\mathbf{Q}} \ \gamma \left\| \mathbf{H} - \mathbf{X}^{i+1} \right\|_2^2 + \lambda \|\mathbf{H}\|_p^p \tag{A7}$$

From the iterative reweighted algorithm, the approximate solution of each iteration can be obtained as follows (**Equation A8**):

$$\mathbf{H}^{k+1} = \min_{\mathbf{V}} \ \gamma \left\| \mathbf{H} - \mathbf{X}^{i+1} \right\|_2^2 + \sum_{k=1}^n \lambda p \left( \left| H_k^i \right| + \varepsilon \right)^{p-1} \left| \mathbf{H}_k \right| \tag{A8}$$

In **Equation A8**, by setting $t_i^{k+1} = \lambda p \left( \left| H_i^k \right| + \varepsilon \right)^{p-1}$, it can be further rewritten into the form of the L1-norm, which can be solved via soft-thresholding calculation, as shown in **Equation A9**:

$$\mathbf{H}^{k+1} = \min_{\mathbf{V}} \ \gamma \left\| \mathbf{H} - \mathbf{X}^{i+1} \right\|_2^2 + \sum_{k=1}^n t_k^{i+1} \left| H_k \right| \tag{A9}$$

The above **Equation A9** can be calculated using the one-dimensional soft-thresholding function, and the result is obtained as follows (**Equation A10**):

$$\begin{aligned}
\mathbf{H}^{i+1} &= \mathrm{shrink}\left(\mathbf{X}^{k+1}, \frac{\mathbf{t}^{i+1}\gamma}{\lambda}\right) \\
&= \max\left\{\mathbf{X}^{i+1} - \frac{\mathbf{t}^{i+1}\gamma}{\lambda}, 0\right\} \bullet \mathrm{sign}\left(\mathbf{X}^{i+1}\right)
\end{aligned}$$

(A10)

Where $\mathrm{sign}(\bullet)$ is the sign function.

The solution for $\mu$ in **Equation A2** can be directly obtained using the gradient descent method in **Equation A11**.

$$\mu^{i+1} = \mu^{i} + \left(\mathbf{Lm}^{i+1} - \mathbf{H}^{i+1}\right)$$

(A11)